metals

MDPI

Supplementary Material

Corrosion and Corrosion Fatigue Characteristics of 316L Stainless Steel Fabricated by Laser Powder Bed Fusion

Balachander Gnanasekaran [1], Jie Song [2,3,*], Vijay Vasudevan [2,4] and Yao Fu [1,3,*]

[1] Department of Aerospace Engineering & Engineering Mechanics, University of Cincinnati, Cincinnati, OH 45221, USA; gnanasbr@mail.uc.edu
[2] Department of Mechanical and Materials Science Engineering, University of Cincinnati, Cincinnati, OH 45221, USA; vasudevk@ucmail.uc.edu
[3] Department of Aerospace and Ocean Engineering, Virginia Tech, Blacksburg, VA 24061, USA
[4] Department of Materials Science Engineering, University of North Texas, Denton, TX 76203, USA
* Correspondence: j.song.thu@gmail.com (J.S.); yaof@vt.edu (Y.F.)

1. Methods and Materials

The microstructures of samples are examined by optical microscopy (OM), scanning electron microscopy (SEM), electron backscatter diffraction (EBSD), and transmission electron microscopy (TEM). The samples for OM and SEM/EBSD are electropolished with a solution of 12.5 vol.% sulfuric acid and 87.5 vol.% methanol at a potential of 50 V at room temperature, and then electrolytically etched in a 10 vol.% saturated oxalic acid solution at 12 V for 90 s. The samples for TEM are prepared using twin-jet polisher with the same solution as electropolishing at a potential of ~20 V and temperature of −30 °C.

Electrochemical Impedance Spectroscopy (EIS) tests were conducted using the Gamry potentiostat. EIS tests were performed for a range of potentials beginning from +50 mV (vs. OCP) up to +500 mV (vs. OCP) in a frequency range of 1 mHz to 100 kHz with 10 points/decade using 10 mV sinusoidal potential. Before EIS, the samples are allowed to passivate at the selected potential for 3 h.

2. Results

2.1. Microstructure Characterization

Figure S1 shows optical microscope images of the XY surface (perpendicular to the building direction) of the sample printed under different laser power settings. Images show solidification tracks (marked in the figure) and the change in the scanning direction of 67º is clearly seen between subsequent layers. Porosity in the sample is shown as a dark spot in the OM images. As the power increases, the porosity of the sample decreases by OM images observation, similar to other studies [1]. This is attributed to an increase in energy density which gives rise to higher efficiency in melting and a denser sample. Partial melting of powder can lead to entrapped protective gas and the formation of pores at lower power settings. It can also be observed that as the hatch spacing decreases, porosity decreases. Smaller hatch spacing also creates narrower tracks [2]. Approximate calculations give a track width value of ~80 μm for a hatch spacing of 90 μm and a value of ~50 μm for a hatch spacing of 50 μm. Additionally, the track width slightly increases for a constant hatch spacing as the laser power increases. This is due to the increase in energy density as the laser power increases giving rise to a larger molten pool and width [3].

The EBSD inverse pole graph (IPF) and kernel average misorientation (KAM) on the XY plane of the samples printed at a hatch spacing of 50 μm are shown in Figure S2. With increasing laser power from 150 W to 240 W, the crystal planes parallel to the build platform are gradually oriented towards {101} plane, more apparent at H = 50 μm than at H = 90 μm (Table S1). At H = 50 μm, as the laser power increases the fraction of grain orientations close to 101 planes increases. At 240 W, the fraction of grains oriented towards 101 plane (angle <10°) reaches a maximum of 90%. Similar phenomenon has been found in

316L SS with lower input energy density of 80 J/mm^3 by changing the scan strategy. The fiber like texture can be formed with a 67° rotation scan in Ni-25 at.% Mo alloys [4]. However, the fibers are aligned along ⟨001⟩ direction instead of ⟨101⟩ direction as in our study.

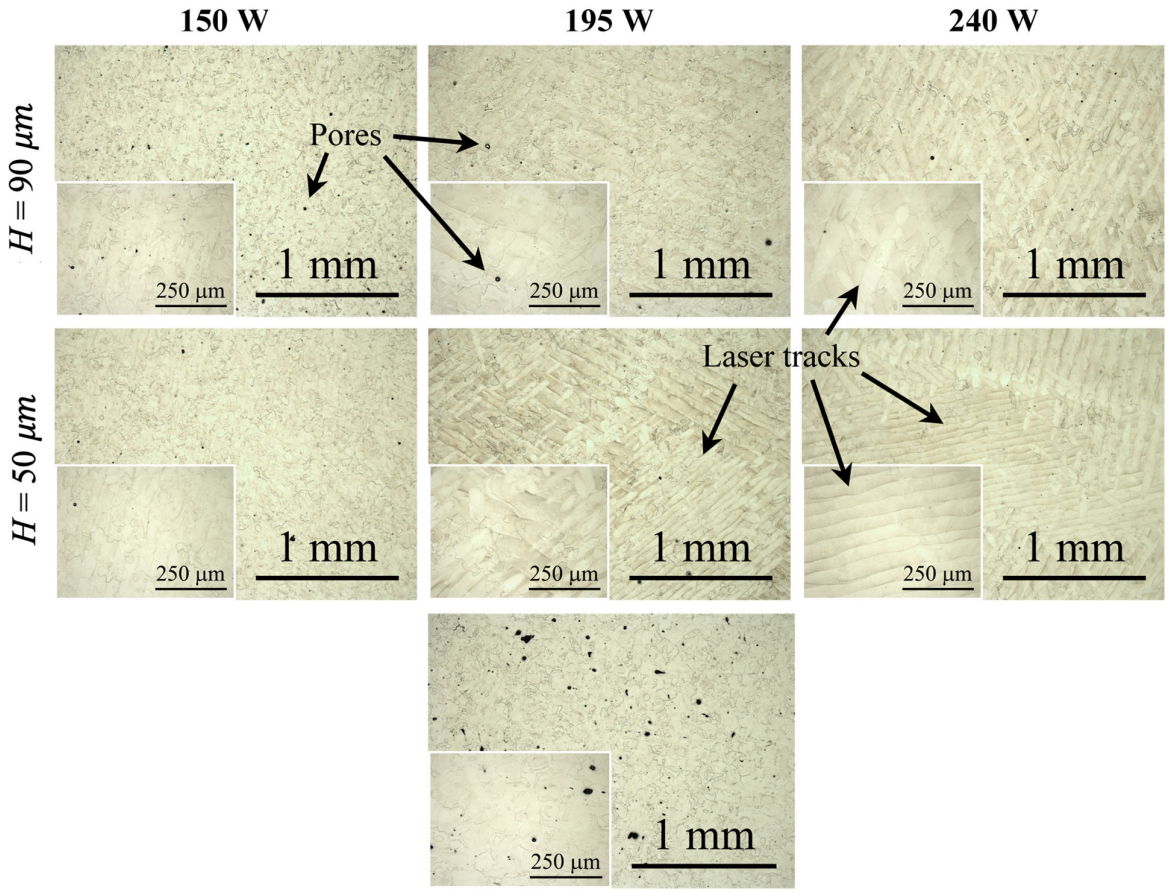

Figure S1. Optical microscopy (OM) images of specimens printed with an increasing laser power from 150 W to 240 W at *H* = 90 μm (**upper row**) and H = 50 μm (**middle row**) and sample 7 (**bottom row**).

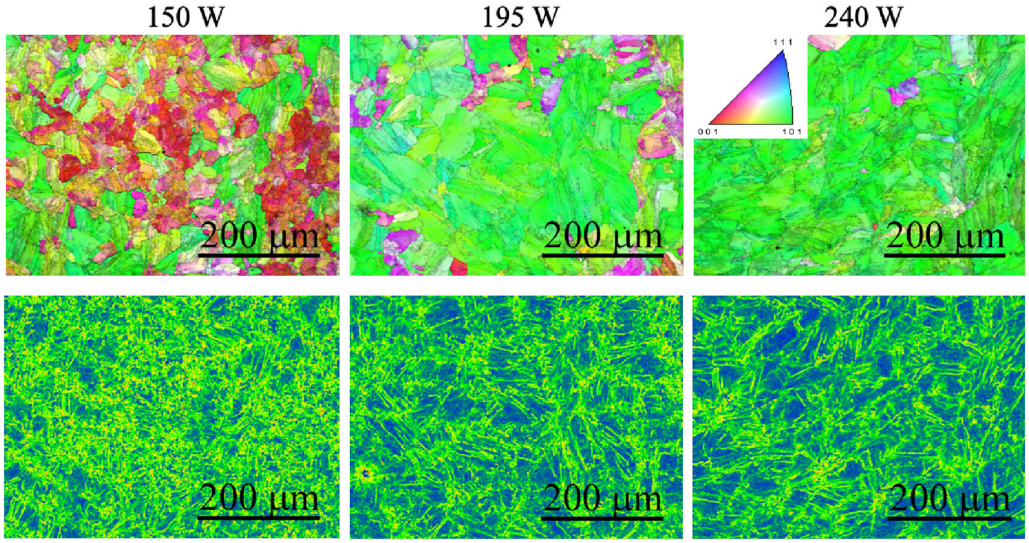

Figure S2. (**Upper panel**) EBSD-IPF images and (**bottom panel**) kernel average misorientation (KAM) images generated with a step size of 0.15 µm and a threshold angle of 5° that indicate the grain orientation, measured on the XY plane at *H* = 50 µm with an increasing laser power from 150 W to 240 W.

The KAM image gives the average misorientation of a point in the grain with respect to neighboring points, which is an indication of dislocation density. A decrease in misorientation and thus dislocation density (plastic strain) can be found in the sample, most likely due to the lower cooling rate at a reduced hatch spacing and at a higher laser power. The change in the misorientation and grain size with printing parameters are also summarized in Table S1. At a lower hatch spacing, misorientation decreases in a more linear manner as laser power increases. For a hatch spacing of 90 µm, the decrease is not linear. As the laser power increases from 150 W to 195 W, KAM decreases slightly while from 195 W to 240 W there is a prominent decrease. With increasing laser power, the grain size only slightly increases from ~12 µm to ~15 µm at *H* = 90 µm, yet at *H* = 50 µm the increase is significant (from ~11 µm to ~27 µm). Under all LPBF conditions, the average grain size is larger than that of the conventional 316L SS.

Table S1. The change in average grain size and KAM with printing parameters.

Power (*P*)	Hatch Spacing (*H*)	Average Grain Size	KAM
150 W	90 µm	12.22	1.12
195 W	90 µm	14.23	1.10
240 W	90 µm	15.21	0.95
150 W	50 µm	11.41	1.16
195 W	50 µm	18.87	0.98
240 W	50 µm	26.89	0.81
	Conventional	8.25	0.37

The planes parallel to the build direction have relatively even distribution of crystallographic planes (Figure 8a in main text). The growth of grains passes through the fusion line, which are generally aligned along the build direction. The columnar/cellular subgrains are characterized by high density of dislocation networks Figure 8b in main text and Figure S3). No precipitates and chemical segregation were found around the dislocation network or within the cells. It is also confirmed that the columnar subgrains grow in the ⟨100⟩ direction by the SAD pattern in TEM analysis (Figure S3).

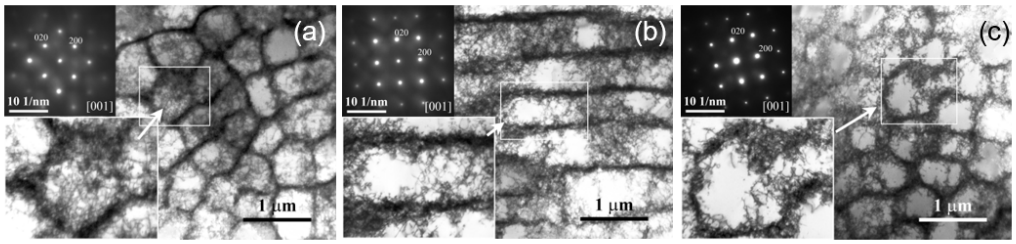

Figure S3. TEM images of subgrains showing (**a**) cellular and (**b**) columnar structure at the cross section.

6.2. Electrochemical Impedance Spectroscopy (EIS) for Passive Film Characteristics

The passive film characteristics are analyzed using EIS within the passivation regime at various potentials. The recorded EIS spectra at 200, 300, and 400 mV are shown in Figure S4. The impedance spectra are analyzed using the equivalent electrical circuit commonly used for passive film. The total impedance of the equivalent electrical circuit is given by [5]:

$$Z = R_! + 1/\&1/R_" + Y_\#(j\omega)^{\$-} \quad \text{(S1)}$$

where R_s and R_p represents the resistance of the solution and the charge transfer resistance of the interface, respectively. Q is the constant phase element with impedance $Z_! = [Y_"(j\omega)^\#]^{\$\%}$, where $Y_"$ and n are two parameters of Q. The fitted parameters are listed in *Table S2*. Both the conventional and LPBF samples show an increase in the passive film resistance up to ~300 mV before decreasing and showing fluctuations. At lower potentials, the LPBF-XZ sample has a slightly higher resistance compared to LPBF-XY and conventional samples. At higher potentials, the difference in resistances of passive films for LPBF-XZ, LPBF-XY and AR is very small. It is also seen that as the voltage increases the stability of the passive film decreases. This is to be expected since at higher voltages, metastable pitting occurs more frequently, and passive film is not able to repassivate quickly enough to show considerable reduction in current.

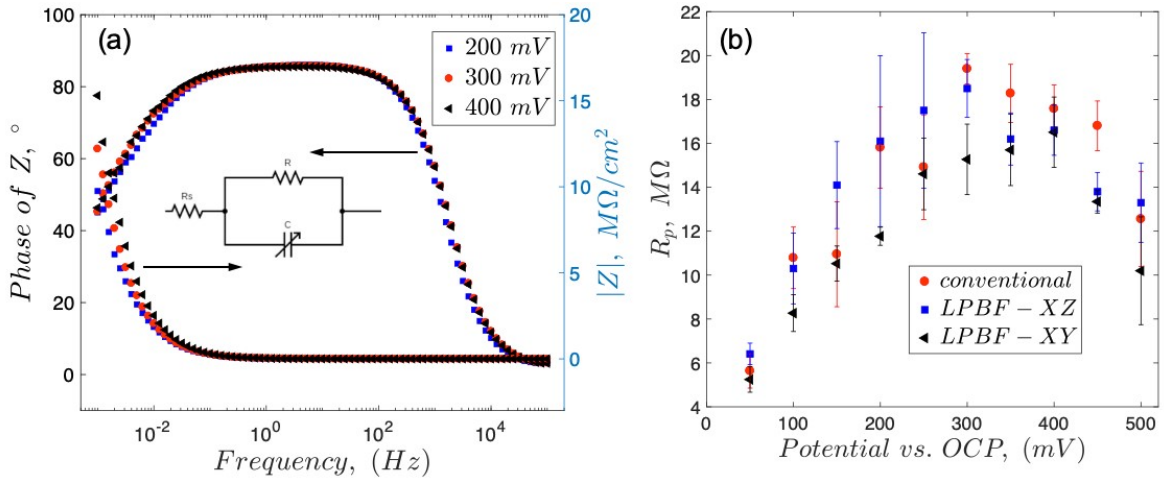

Figure S4. (**a**) Examples of (**a**) Bode plots for the passive films of the LPBF-XY sample formed at the various passive potentials, and (**b**) the extracted interface transfer resistance from the EIS spectra.

Table S2. Characteristics of the passive film formed and tested at different potentials, obtained by fitting to the equivalent circuit.

Potentials (mV)	**Resistance of Solution, R_s (ohm)**			**Charge Transfer Resistance, R (Mohm)**		
	Conventional	**AM-XY**	AM-XZ	Conventional	AM-XY	AM-XZ
50	21.7 ± 3.3	24.1 ± 6.1	19.2 ± 0.6	5.64 ± 0.8	5.4 ± 0.6	6.4 ± 0.5
100	21.4 ± 3.2	20.7 ± 2.1	18.9 ± 0.2	10.8 ± 1.4	8.3 ± 0.8	10.3 ± 1.6
150	19.2 ± 0.6	21.5 ± 2.9	18.9 ± 0.1	10.9 ± 2.4	10.5 ± 0.8	14.1 ± 2.0
200	18.8 ± 0.1	20.3 ± 2.0	19.0 ± 0.2	15.8 ± 1.9	11.8 ± 0.4	16.1 ± 3.9
250	18.9 ± 0.0	22.0 ± 5.0	19.4 ± 0.7	14.9 ± 2.4	14.6 ± 1.6	17.5 ± 3.5
300	20.2 ± 1.0	28.0 ± 11.0	19.2 ± 0.2	19.4 ± 6.9	15.3 ± 1.6	18.5 ± 1.3
350	23.8 ± 5.8	21.0 ± 2.6	19.2 ± 0.5	18.3 ± 1.3	15.7 ± 1.3	16.2 ± 1.2
400	22.1 ± 4.1	22.0 ± 3.3	19.1 ± 0.4	17.6 ± 1.1	16.5 ± 1.6	16.6 ± 1.1
450	29.6 ± 11.8	19.3 ± 0.5	19.0 ± 0.04	16.8 ± 1.1	13.3 ± 0.5	13.8 ± 0.9
500	19.1 ± 0.7	24.1 ± 3.2	19.1 ± 0.3	12.6 ± 2.2	10.2 ± 2.5	13.3 ± 1.8
Potentials (mV)	Constant Phase Element Parameter, *Y0* (10-6 Ω-1m-2sn)			Constant Phase Element Parameter, *n*		
50	*Conventional*	*AM-XY*	*AM-XZ*	*Conventional*	*AM-XY*	*AM-XZ*
	9.1 ± 0.02	9.8 ± 0.6	8.8 ± 0.3	0.94 ± 0.01	0.94 ± 0.01	0.93 ± 0.00
100	7.7 ± 0.48	8.6 ± 0.2	7.7 ± 0.5	0.93 ± 0.00	0.94 ± 0.00	0.93 ± 0.01
150	7.5 ± 0.69	7.4 ± 0.3	6.9 ± 0.3	0.94 ± 0.00	0.94 ± 0.00	0.93 ± 0.00
200	6.4 ± 0.26	7.1 ± 0.2	6.3 ± 0.4	0.94 ± 0.00	0.94 ± 0.00	0.94 ± 0.01
250	6.1 ± 0.36	6.4 ± 0.4	5.8 ± 0.4	0.94 ± 0.00	0.95 ± 0.00	0.94 ± 0.00
300	5.3 ± 0.08	6.2 ± 0.3	5.6 ± 0.4	0.94 ± 0.00	0.95 ± 0.00	0.94 ± 0.01
350	5.2 ± 0.26	5.5 ± 0.2	5.8 ± 0.4	0.94 ± 0.00	0.95 ± 0.00	0.94 ± 0.00
400	5.1 ± 0.09	5.3 ± 0.2	5.1 ± 0.3	0.94 ± 0.01	0.94 ± 0.01	0.94 ± 0.00
450	5.1 ± 0.05	5.3 ± 0.2	5.3 ± 0.2	0.94 ± 0.00	0.94 ± 0.00	0.94 ± 0.00
500	5.0 ± 0.10	5.2 ± 0.3	4.9 ± 0.1	0.94 ± 0.00	0.94 ± 0.00	0.94 ± 0.01

References:

1. Sander, G.; Thomas, S.; Cruz, V.; Jurg, M.; Birbilis, N.; Gao, X.; Brameld, M.; Hutchinson, C.R. On The Corrosion and Metastable Pitting Characteristics of 316L Stainless Steel Produced by Selective Laser Melting. *J. Electrochem. Soc.* **2017,** *164*, C250–C257.
2. Dong, Z.; Liu, Y.; Wen, W.; Ge, J.; Liang, J. Effect of Hatch Spacing on Melt Pool and As-built Quality During Selective Laser Melting of Stainless Steel: Modeling and Experimental Approaches. *Materials* **2019**, *12*, 50. https://doi.org/10.3390/ma12010050
3. Hu, Z.; Nagarajan, B.; Song, X.; Huang, R.; Zhai, W.; Wei, J. Formation of SS316L Single Tracks in Micro Selective Laser Melting: Surface, Geometry, and Defects. *Adv. Mater. Sci. Eng.* **2019,** *2019***,** 9451406.
4. Sun, S.-H.; Hagihara, K.; Nakano, T. Effect of scanning strategy on texture formation in Ni25at.%Mo alloys fabricated by selective laser melting. *Mater. Des.* **2018**, *140*, 307–316.
5. Fattah-alhosseini, S.; Taheri Shoja, B.; Zebardast, H.; Mohamadian Samim, P. An Electrochemical Impedance Spectroscopic Study of the Passive State on AISI 304 Stainless Steel. *Int. J. Electrochem. Sci.* **2011**, *2011*, 152143.